



A new strategy for estimating geophysical parameters from InSAR data: Application to the Krafla central volcano in Iceland

S. T. Ali and K. L. Feigl

Department of Geoscience, University of Wisconsin–Madison, 1215 West Dayton Street, Madison, Wisconsin 53706, USA (stali@geology.wisc.edu; feigl@wisc.edu)

[1] We develop, validate, and apply a new strategy for estimating parameters in a geophysical model from interferometric synthetic aperture radar (InSAR) measurements. The observable quantity is a particular component of the deformation gradient tensor, defined as the derivative of the change in range with respect to the easting coordinate. This range change gradient is derived from wrapped phase data by a quadtree resampling procedure. Since the range change gradient is a continuous function of position, the strategy avoids the pitfalls associated with phase unwrapping techniques. To quantify the misfit between the observed and modeled values of the range gradient, the objective function calculates the cost as the absolute value of their difference, averaged over all samples. To minimize the objective function, we use a simulated annealing algorithm. This algorithm requires several thousand evaluations of the fitting function to find the optimum solution: the estimate of the model parameters that produces the lowest value of cost. For computational efficiency, we approximate the fitting function using a Taylor series. The simulated annealing algorithm then evaluates the approximate and fast version of the fitting function. After performing these two steps several times, the scheme converges, typically in a few iterations. We apply the strategy to Krafla central volcano in Iceland. Using a data set composed of eight interferometric pairs acquired by the ERS-1 and ERS-2 satellites over a 6-year interval between 1993 and 1999, we estimate the four parameters in a Mogi model. Results suggest a source at 4.98 ± 0.21 km depth and a deflation rate that decays exponentially over the interval, in agreement with previous studies.

Components: 9900 words, 12 figures, 4 tables.

Keywords: InSAR; Krafla central volcano; nonlinear inversion.

Index Terms: 1209 Geodesy and Gravity: Tectonic deformation (6924); 1241 Geodesy and Gravity: Satellite geodesy: technical issues (6994, 7969); 3260 Mathematical Geophysics: Inverse theory.

Received 20 February 2012; **Revised** 8 May 2012; **Accepted** 8 May 2012; **Published** 8 June 2012.

Ali, S. T., and K. L. Feigl (2012), A new strategy for estimating geophysical parameters from InSAR data: Application to the Krafla central volcano in Iceland, *Geochem. Geophys. Geosyst.*, 13, Q06005, doi:10.1029/2012GC004112.

1. Introduction

[2] Interferometric Synthetic Aperture Radar (InSAR) has become an indispensable tool for estimating parameters in geophysical models related to earthquake

and volcano deformation [Massonnet and Feigl, 1998; Wright, 2002]. The standard approach involves two steps. In the first step, an algorithm is used to unwrap the observed phase change (in cycles) to obtain the unambiguous range change

(in meters). In the second step, inverse modeling is used to estimate parameters using optimization [e.g., *Hetland et al.*, 2012]. In this paper we propose, develop, validate and apply a strategy that avoids the need for unwrapping the observed phase and requires only a few evaluations of the exact fitting function. After validating the strategy using simulated interferograms, we apply it to estimate parameters associated with the magmatic source beneath the Krafla central volcano using radar data acquired between 1993 and 1999.

2. Observable Quantity: Gradient of Range Change

[3] To build a data set for the inversion, we calculate the gradient of range change while simultaneously resampling (but not unwrapping) with a quadtree algorithm called PHA2QLS (K. L. Feigl and P. Sobol, PHA2QLS.C: a computer program to compress images of wrapped phase by simultaneously estimating gradients and quadtree resampling, manuscript in preparation, 2012). The quadtree algorithm, originally developed for image compression [e.g., *Samet*, 1984], has been applied previously to unwrapped interferograms, i.e., the scalar field of range change (in millimeters) in previous studies [*Jonsson et al.*, 2002]. *Simons et al.* [2002] use a similar approach, based on the curvature of the unwrapped interferogram. Here, we apply the PHA2QLS quadtree algorithm to wrapped phase. For each square patch of pixels, the quadtree algorithm estimates three parameters: the circular mean direction, the partial derivative of phase with respect to the easting coordinate, and the partial derivative of phase with respect to the northing coordinate. The two derivatives are equivalent to the two horizontal components of the range change gradient. In a given horizontal direction, the range change gradient is proportional to the wave number of the fringe pattern and thus inversely proportional to the distance between adjacent fringes. The misfit to this simple three-parameter empirical model for a planar phase ramp, as measured by the circular mean deviation [*Mardia and Jupp*, 2000] of the wrapped residual phase, is the criterion for subdividing the patch in the quadtree algorithm. If the misfit exceeds a pre-set threshold (e.g., 0.25 cycles), then the patch is subdivided into four more square patches. If, on the other hand, the misfit is less than or equal to the threshold value, then the value of the partial derivative of phase with respect to the easting coordinate is recorded for the patch. The smallest allowable patch

is 2 pixels in length by 2 pixels in width. This process continues recursively until completion. The quadtree procedure thus provides a set of range gradient values that are suitable for inversion.

[4] The resulting data set has several advantages. The resampled data set is smaller than the complete data set, typically by a factor of 10 to 1000. For example, we consider a 4×4 patch composed of 16 pixels. If the 3-parameter planar model fits the 16 phase values to within 0.25 cycles, then the resampling algorithm retains a single value, the range gradient, to represent the deformation field in the patch. In this example, the compression factor is 16. The resampled data set therefore includes only those patches with high spatial coherence, one measure of interferometric quality. The gradients are estimated over patches for which the size adapts to the variations in the data. We illustrate the procedure below.

[5] The quadtree procedure provides three scalar fields corresponding to the values of the three parameters estimated for each patch: (a) the circular mean phase, (b) the discrete derivative of range change with respect to the easting coordinate, and (c) the discrete derivative of range change with respect to the northing coordinate. Since each of these fields is derived from the same original field of wrapped phase, any one of them can be used to represent the deformation field. The range gradient offers a number of advantages as an observable quantity for subsequent analysis. Following *Sandwell and Price* [1998], we take the discrete derivative of range change $\Delta\rho$ with respect to a horizontal coordinate in position X to define the observable quantity for the k th pixel as:

$$\psi^k = \frac{\Delta\rho^{(k+1)} - \Delta\rho^{(k-1)}}{X^{(k+1)} - X^{(k-1)}} \quad (1)$$

Unlike wrapped phase change, the range change gradient ψ is continuous and differentiable [*Sandwell and Price*, 1998]. Using the gradient of range change as an observable quantity avoids the pitfalls of phase unwrapping, as discussed by *Feigl and Thurber* [2009]. While range change is one component of the displacement vector, its gradient is one component of the “deformation gradient” tensor [*Malvern*, 1969]. For example a difference of 0.1 cycles in phase or 2.8 mm in range change over the 100 m distance between adjacent pixels in the interferogram corresponds to a range gradient of $\psi \sim 2.8 \times 10^{-5}$. The fundamental condition for InSAR implies that the horizontal gradient of

wrapped range change cannot exceed 0.5 cycle per pixel in absolute value, e.g., 1.4×10^{-4} for the ERS-1 and ERS-2 radar sensors [Massonnet and Feigl, 1998]. If the range gradient exceeds this “gradient limit” in absolute value, then the corresponding pixel in the interferogram will show no correlation and will thus be excluded by the quadtree resampling.

3. Defining the Forward Model as a Fitting Function

[6] To describe the observed field ψ , we seek a modeled field $\tilde{\psi}$ defined in terms of a set of m parameters \vec{p} . We evaluate the fitting function $\tilde{\psi}(\vec{p})$ at each pixel k over each time interval $[t_i, t_j]$. The fitting function describing the gradient of range change for the k th pixel is defined as

$$\tilde{\psi}^{(k)}(\vec{p}) = \frac{\Delta\rho^{(k+1)}(\vec{p}) - \Delta\rho^{(k-1)}(\vec{p})}{X^{(k+1)} - X^{(k-1)}} \quad (2)$$

where the range change $\Delta\rho$ is defined as

$$\Delta\rho^{(k)} = - \begin{bmatrix} u_E^{(k)}(\vec{p}) & u_N^{(k)}(\vec{p}) & u_U^{(k)}(\vec{p}) \end{bmatrix} \begin{bmatrix} \hat{s}_E^{(k)} \\ \hat{s}_N^{(k)} \\ \hat{s}_U^{(k)} \end{bmatrix} \quad (3)$$

where subscripts E , N and U denote the east, north and upward components, respectively, of the displacement vector \vec{u} and the unit vector \hat{s} pointing from the pixel to the satellite. Although a choice of coordinate system for differentiation is arbitrary, only one component of the gradient is required to represent the information in the interferogram. We choose the eastward component of the range gradient for simplicity.

[7] Following previous studies [Savage, 1988; Fialko, 2004; Feigl and Thurber, 2009], we write the range change $\Delta\rho$ at the i th temporal epoch t_i for the k th pixel located at position $\vec{X}^{(k)}$ as a separable function

$$\Delta\rho^{(k)}(t_i) = f(t_i)g(\vec{X}^{(k)}) + h_i(\vec{X}^{(k)}) \quad (4)$$

where $f(t)$ is a temporal function describing the deformation field’s dependence on time, $g(\vec{X}^{(k)})$ is a mapping function describing the dependence on position $\vec{X}^{(k)}$, and $h_i(\vec{X}^{(k)})$ is a function describing “nuisance effects” due to satellite orbits and atmospheric propagation. Taking the discrete derivative

with respect to a spatial coordinate X_1 (easting), we find the gradient of range change

$$\begin{aligned} \psi^{(k)}(t_i) &= \frac{\delta\Delta\rho}{\delta X_1} \\ &= f(t_i) \left[\frac{g(\vec{X}^{(k+1)}) - g(\vec{X}^{(k)})}{X_1^{(k+1)} - X_1^{(k)}} \right] \\ &\quad + \frac{h_i(\vec{X}^{(k+1)}) - h_i(\vec{X}^{(k)})}{X_1^{(k+1)} - X_1^{(k)}} \end{aligned} \quad (5)$$

In our subsequent analysis of volcanic deformation, we use a mapping function $g(\vec{X}^{(k)})$ attributed to Mogi [1958] to describe the displacement of an observation point with coordinates $\vec{X}^{(k)}$ located at the surface of an elastic halfspace. The source of deformation is a spherical cavity located at $\vec{X}^{(Mogi)}$. Our formulation of the Mogi source describes the east, north, and vertical components of displacement \vec{u} at $\vec{X}^{(k)}$ as

$$u_E = \frac{\Delta X_1 \Delta V (\nu - 1)}{\pi (\Delta X_1^2 + \Delta X_2^2 + d^2)^{3/2}} \quad (6)$$

$$u_N = \frac{\Delta X_2 \Delta V (\nu - 1)}{\pi (\Delta X_1^2 + \Delta X_2^2 + d^2)^{3/2}} \quad (7)$$

$$u_U = \frac{-d \Delta V (\nu - 1)}{\pi (\Delta X_1^2 + \Delta X_2^2 + d^2)^{3/2}} \quad (8)$$

where ΔV is the volume change, ν is Poisson’s ratio, $\Delta\vec{X} = \vec{X}^{(k)} - \vec{X}^{(Mogi)}$, and $d = |X_3^{(Mogi)}|$.

[8] To describe the temporal evolution of the deformation, we assume a linear function $f(t_i) = t_i - t_0$ where t_0 is an arbitrary reference epoch. The rate of deformation thus is constant and the volume change ΔV becomes an annual rate $\Delta V/\Delta t$.

[9] The field of range change gradient values is sensitive to processes that are not related to deformation on the ground. For example, inaccurate knowledge of the satellite’s orbital trajectory can contribute to the range gradient at the level of $\sim 10^{-7}$ [Kohlhase et al., 2003]. In the case of a volcano, though, the orbital effect is negligible compared to the deformation signal. Since the orbital effect varies little over spatial scales shorter than ~ 10 km, it would appear as an additive constant in the expression for the range change gradient ψ . It could, in principle, be modeled by estimating additional

parameters to describe the orbital adjustments. The nuisance effect at the i th epoch t_i is simply described as a linear function of the topographic elevation, i.e., the vertical component of the position coordinate such that

$$h_i(\vec{X}^{(k)}) = h_i(X_3^{(k)} - X_3^{(0)}) \quad (9)$$

where $\vec{X}^{(0)}$ is an arbitrary reference location. Finally, we write the difference in the gradient of range change between epochs t_i and t_j as

$$\Delta\psi_i^{(k)} = D_{ij}^{(k)}\psi^{(k)}(t_j) \quad (10)$$

where $D_{ij}^{(k)}$ is a incidence matrix with c rows and q columns composed of values $\{-1, 0, +1\}$, as described by *Feigl and Thurber* [2009, equation (2)].

4. Inverse Problem

[10] Given a set of observed values ψ and modeled values $\tilde{\psi}$ of the gradient of range change, we seek to minimize the objective (cost) function defined as the mean of the angular deviations between the two. For wrapped phase, the deviation in cycles between the observed value ϕ and the modeled value $\tilde{\phi}$ is:

$$\omega = \text{arc}(\phi, \tilde{\phi}) = \frac{1}{2} - \left| \frac{1}{2} - \left| \phi - \tilde{\phi} \right| \right| \quad (11)$$

where the *arc* function is defined by *Feigl and Thurber* [2009, equations (14)–(16), and references therein; *Mardia and Jupp*, 2000; *Nikolaidis and Pitas*, 1998]. The objective function is an L_1 norm that is equivalent to the circular mean deviation of the angular residuals (phase in cycles or phase gradients in cycles/pixel) if their (circular) mean direction is negligible [*Feigl and Thurber*, 2009]. The mean deviation (averaged over all values in the resampled data set) is the cost, i.e., the objective function to be minimized, is defined as:

$$\bar{\omega}' = \frac{1}{n} \sum_{k=1}^n \text{arc}(\psi^{(k)}, \tilde{\psi}^{(k)}) \quad (12)$$

Like the range gradient ψ , the cost $\bar{\omega}'$ is dimensionless.

[11] To minimize the objective function $\bar{\omega}'$ and estimate the optimal values of the parameters \vec{p} , we employ the simulated annealing algorithm [*Kirkpatrick et al.*, 1983], as implemented by *Goffe*

[1996]. This algorithm requires evaluating the objective function, and thus the fitting function, many times. Typically, the number of evaluations is of the order of $\sim 10^4$ for problems like the one considered here. In order to reduce the computational cost of the forward problem during simulated annealing, we approximate the fitting function by a second-order Taylor series:

$$\tilde{\psi}(\vec{p}) = \tilde{\psi}(\vec{p}_0) + \sum_{i=1}^m \left[\frac{\tilde{\psi}(p_0)'}{1}(p_i - p_0) + \frac{\tilde{\psi}(p_0)''}{2}(p_i - p_0)^2 \right] \quad (13)$$

where p_0 is the initial estimate and p the trial value of a single parameter. The derivatives $\tilde{\psi}(p_0)'$ and $\tilde{\psi}(p_0)''$ with respect to each parameter are evaluated numerically using finite difference formulas around \vec{p}_0 before each iteration. For computational efficiency, we neglect second-order mixed derivatives of $\tilde{\psi}$ with respect to more than one parameter. Evaluation of the approximated fitting function $\tilde{\psi}(\vec{p})$, thus involves only matrix-vector multiplication and vector addition, in equation (13).

[12] Using the approximated fitting function changes the shape of the objective function being minimized. Consequently, the final estimate may not be the same as the one estimated using the exact fitting function. To alleviate this problem, a few iterations of the simulated annealing procedure described above are required. At the end of first iteration, the final estimate is used as the initial estimate for the subsequent iteration and the procedure is repeated until the estimated parameters converge to a steady value. The total number of evaluations of the exact fitting function is $l(2m + 1)$, where l is the number of iterations and m is the number of free parameters being estimated. Of these, the $2m + 1$ evaluations required for the second-order Taylor approximation can be performed in parallel. This approach works well as long as the number of parameters m is small, as is the case here.

[13] To summarize, the main steps involved in the procedure are:

[14] (a) Calculate partial derivatives using central difference formulas needed for the second-order Taylor approximation of the fitting function.

[15] (b) Optimize the objective function using the approximated fitting function via simulated annealing.

[16] (c) Use optimized estimate \vec{p}_1 as the new initial estimate \vec{p}_0 .

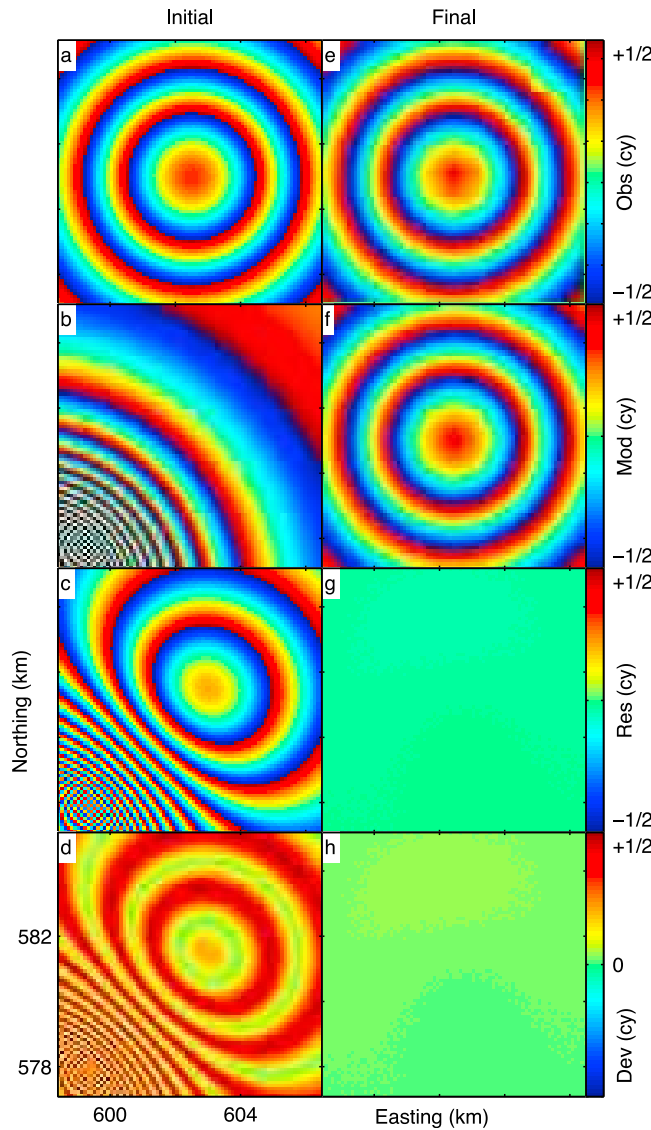


Figure 1. Wrapped phase values for the validation experiment without noise. (a) Phase values ϕ simulated using the optimal values of the parameters, (b) modeled phase values $\tilde{\phi}$ calculated from the initial estimate, (c) initial residual phase values θ formed by subtracting the initial modeled phase values from the simulated phase values, (d) deviations ω for the initial estimate, (e) simulated phase values after quadtree resampling, (f) modeled phase values calculated from the final estimate, (g) final residual phase values formed by subtracting the final modeled values from the simulated phase values, and (h) deviations for the final estimate. In Figures 1a–1c and 1e–1g, one colored fringe corresponds to one cycle of phase change, or 28 mm of range change. In Figures 1d and 1h, the colors denote the deviation in phase. Coordinates are easting and northing in a Lambert Conformal Conic projection defined with two parallels and the ISN93 datum [Rennen, 2004a, 2004b].

[17] (d) Repeat steps (a) through (c) until convergence, i.e., the parameter estimates achieve a steady value.

5. Validation

[18] To validate the strategy, we perform experiments with simulated data, with and without noise. In the first experiment, we generate a set of

wrapped phase values ϕ (Figure 1a) due to deformation caused by a Mogi source buried at depth using a set of parameters \vec{p}_{opt} , as listed in Table 1. After taking the gradient of range change and simultaneous resampling (from 6400 pixels to 556 patches, shown in Figure 2a), we estimate parameters of the model using the methodology described above. To demonstrate the strategy, we:

Table 1. Initial and Final Parameter Estimates for the Validation Experiments

Experiment	Parameter	Optimal p_{opt}	Initial p_0	Final p_1	LB p_L	UB p_U	Adjust.	Uncert. σ
Without noise	Easting (km)	602.5	597.5	602.4990	597.5	607.5	0.9 (m)	1.7 (m)
	Northing (km)	581.0	576.0	580.9993	576.0	586.0	0.6 (m)	2.8 (m)
	Depth (km)	5.0	2.5	4.9983	2.5	7.5	1.6 (m)	5.8 (m)
	ΔV ($10^6 \text{ m}^3/\text{yr}$)	-2.5	-5.0	-2.4969	-5.0	0.0	0.003	0.008
With spatially correlated noise	Easting (km)	602.5	597.5	602.5540	597.5	607.5	54.0 (m)	86.9 (m)
	Northing (km)	581.0	576.0	581.0795	576.0	586.0	79.5 (m)	212.6 (m)
	Depth (km)	5.0	2.5	4.6766	2.5	7.5	323.4 (m)	418.8 (m)
	$\Delta V/\Delta t$ ($10^6 \text{ m}^3/\text{yr}$)	-2.5	-5.0	-2.0840	-5.0	0.0	0.416	0.426

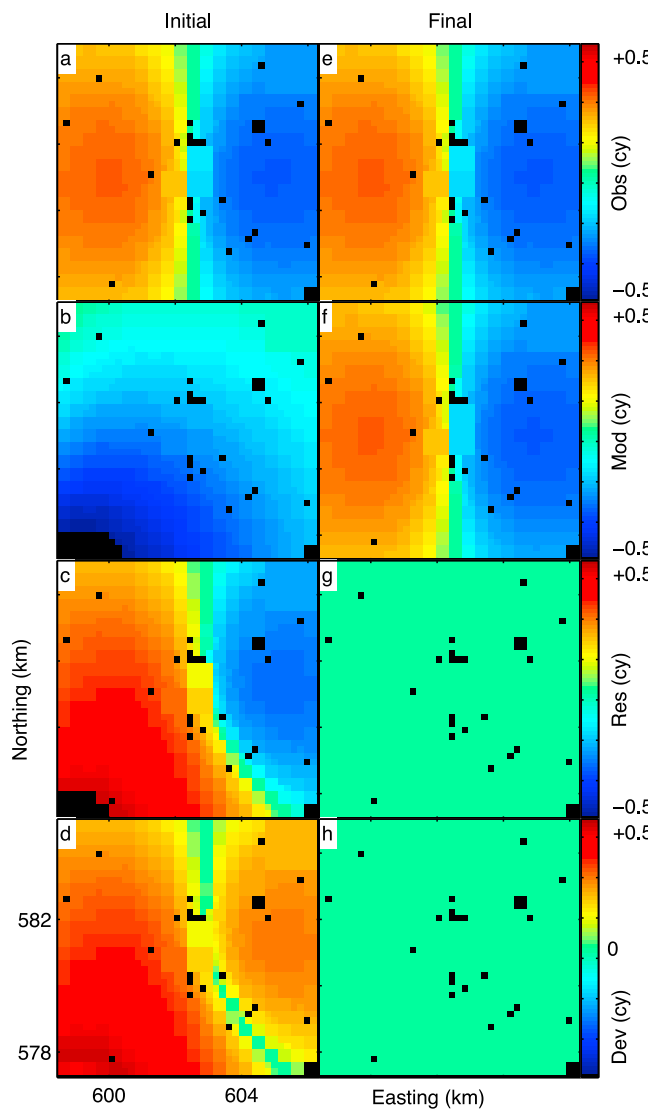


Figure 2. Gradient of range change values for validation experiment without noise. (a) Values ψ calculated from simulated phase during quadtree resampling; (b) modeled values ψ calculated from the initial estimate; (c) initial residual values formed by subtracting the initial modeled values from the simulated values; (d) deviations ω' for the initial estimate; (e) simulated values, repeated for convenience; (f) modeled values calculated from the final estimate; (g) final residual values formed by subtracting the final modeled values from the simulated values; and (h) deviations for the final estimate. A deviation of 0.1 cycles in phase or 2.8 mm in range change over the 100 m distance between pixels in the interferogram corresponds to a range gradient of $\psi \sim 2.8 \times 10^{-5}$. The black color represents patches where gradients are either extreme ($|\psi| > 0.5$ cycles per pixel) or excluded by the quadtree algorithm.

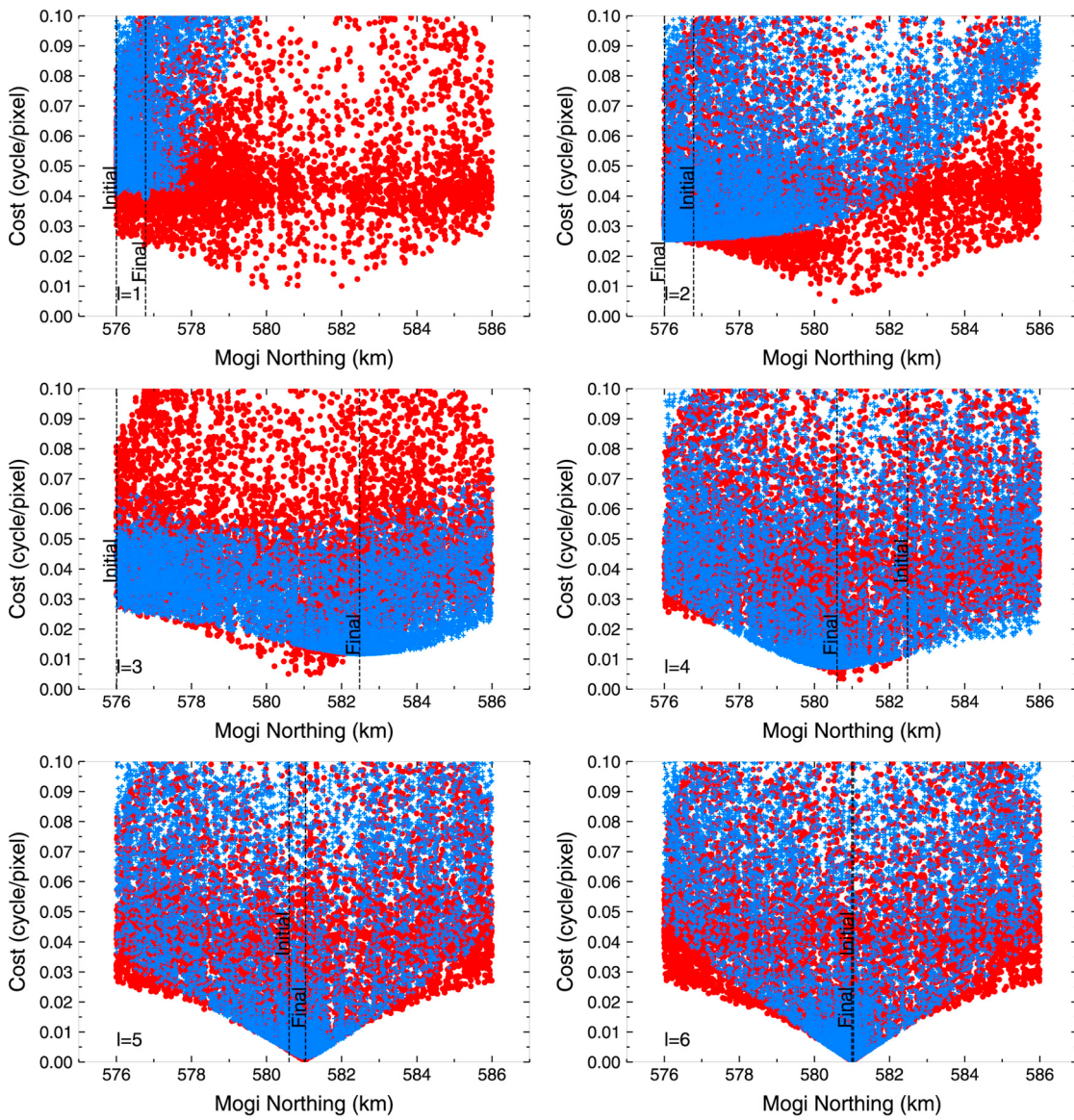


Figure 3. Values of objective function or cost $\bar{\omega}'$ as a function of the Northing parameter for iterations $l = 1$ through $l = 6$. Blue crosses show the cost calculated from the approximated fitting function. Red circles show the cost calculated using the exact fitting function. Vertical dashed lines represent the initial and final estimates of the parameter. Lower and upper bounds for the parameter are 576 km and 586 km, respectively.

(a) choose wide bounds as listed in Table 1, and (b) use the lower bound as the initial estimate \vec{p}_0 . Following the mathematical notation and plotting conventions of Feigl and Thurber [2009], we display the modeled phase values $\tilde{\phi}$ calculated from the initial estimate of the parameter vector \vec{p}_0 in Figure 1b. The residual phase values, calculated by taking the wrapped difference of the simulated observations and the modeled phase values as $\theta = \text{wrap}(\phi - \tilde{\phi})$, appear in Figure 1c. The angular deviations, calculated as $\omega' = \text{arc}(\phi, \tilde{\phi})$ appear in Figure 1d. The corresponding values of the range

gradient appear in Figures 2a–2d: Figure 2a shows values ψ calculated from simulated phase during quadtree resampling, Figure 2b shows modeled values $\tilde{\psi}$, Figure 2c shows residuals $\psi - \tilde{\psi}$, and Figure 2d shows absolute deviations $\omega' = \text{arc}(\psi, \tilde{\psi})$.

[19] On performing the inversion using the approximated fitting function iteratively, we find that the solution converges to the optimal value in $l = 7$ iterations. The total number of evaluations of the exact fitting function is $l(2m + 1) = 7(2(4) + 1) = 63$.

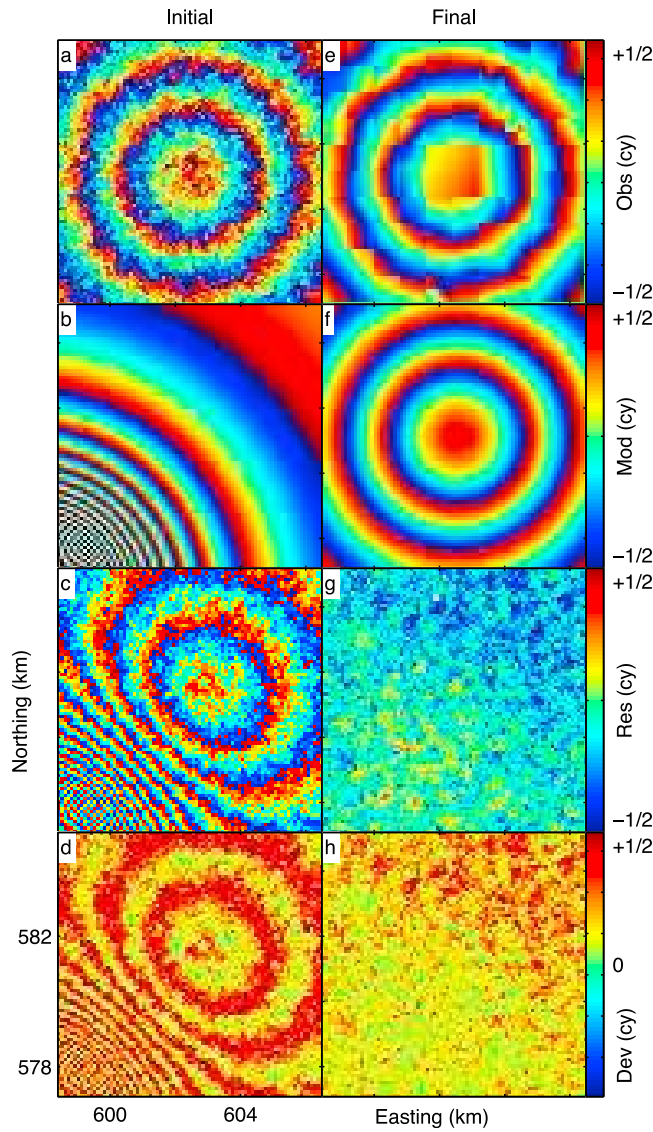


Figure 4. Wrapped phase values for validation experiment with random noise. Plotting conventions as in Figure 1.

The cost decreases from $\bar{\omega}'_0 = 0.08209$ cycles per pixel for the initial estimate \vec{p}_0 to $\bar{\omega}'_1 = 0.00055$ cycles per pixel for the final estimate \vec{p}_1 . The modeled range gradient field calculated from the final estimate (Figure 2f) matches the simulated observations (Figure 2e) quite well. Indeed, the absolute value of the residual range gradient (Figure 2g) is everywhere less than 0.0045 cycles per pixel. Similarly, the deviations ω' shown in Figure 2h have been successfully minimized such that their maximum value is 0.0060 cycles per pixel. To evaluate how well the optimization strategy recovers the original values of the parameters, we also consider the wrapped phase values in the right column of Figure 1. The modeled phase values $\tilde{\phi}$ shown in

Figure 1f match the resampled simulated observations ϕ shown in Figure 1e quite well. Their wrapped residual difference has a nearly constant value of $\theta = -0.13 \pm 0.01$ cycles everywhere in the field, as shown in Figure 1g. Similarly, the angular deviation is $\omega = 0.13 \pm 0.01$ cycle everywhere in the field, as shown in Figure 1h. The standard deviation of the phase residuals is less than the threshold misfit of 0.0625 cycles set as the maximum allowable value of circular mean deviation in the quadtree resampling. The variations in cost with respect to the Northing parameter are shown in Figure 3 as blue crosses. For the purpose of validation, we also plot the cost values using the exact fitting function as red circles. For brevity, plots of cost as a function

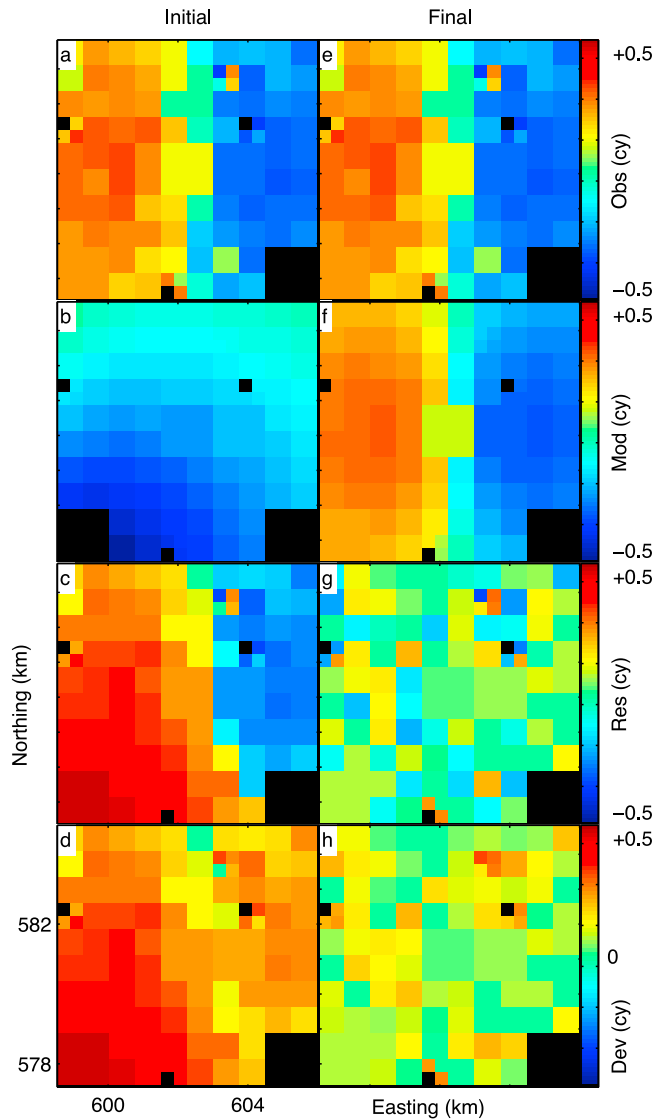


Figure 5. Gradient of range change values for validation experiment with random noise. Plotting conventions as in Figure 2.

of the Easting, Depth and Volume change parameters are not shown.

[20] To calculate uncertainty of estimated parameters, we use bootstrap resampling [Efron and Tibshirani, 1986] to generate 100 random realizations of the data set and thus 100 estimates of the parameter vector \vec{p} . Since we use the approximate fitting function using partial derivatives recorded in the final iteration, the bootstrap does not require any additional evaluations of the exact fitting function. The uncertainty σ for each parameter is simply the sample standard deviation of the 100 estimates, as listed in Table 1. The final estimates \vec{p}_{opt} fall well within the 69% confidence interval $\vec{p}_{opt} \pm \vec{\sigma}$, validating the approach.

[21] In the second experiment, we add spatially correlated noise on length scales of the order of ~ 100 m [Lohman and Simons, 2005] to the simulated data set, and repeat the procedure just described. With added noise, we find that the parameter estimates converge to a steady value in $l = 15$ iterations, requiring a total of $l(2m + 1) = 15(2(4) + 1) = 135$ evaluations of the exact fitting function. The cost decreases from $\bar{\omega}' = 0.0805$ cycles per pixel for the initial estimate to $\bar{\omega}' = 0.0135$ cycles per pixel for the final estimate. The wrapped range change field and its gradient, calculated using the initial and final estimates, along with their residuals and deviations, are shown in Figures 4 and 5, respectively. The final parameter

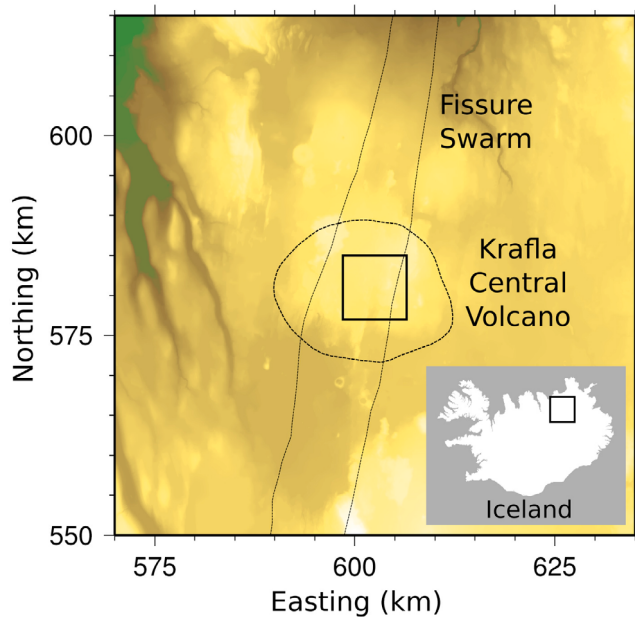


Figure 6. Map showing the location of the Krafla central volcano and the associated fissure swarm. The study area is shown in the rectangular box. Coordinates are Easting and Northing in a Lambert Conformal Conic projection defined with two parallels and the ISN93 datum [Rennen, 2004a, 2004b]. Inset shows Iceland.

estimate \vec{p}_1 agrees with the optimal estimate \vec{p}_{opt} within the bootstrap uncertainties $\vec{\sigma}$, as listed in Table 1, validating the approach.

[22] The estimation procedure just described successfully recovers the original values of parameters in a test using simulated data, both with and without noise. Yet we can imagine cases in which the procedure might fail. In the case where the bounds delimit a portion of the parameter space that includes several possible solutions, the objective function will include multiple local minima. For example, a dike striking due north and dipping 10° to the east and its conjugate striking due south and dipping 10° to the west both provide acceptable solutions. In such cases, the solution will converge to the (nearest) local minimum. In practice, however, we can avoid this situation by finding an initial estimate for the parameter vector \vec{p}_0 by trial and error and then setting the upper and lower bounds around it.

6. Application to the Krafla Central Volcano

[23] The Krafla volcanic system is located within the Northern Volcanic Zone (NVZ) of Iceland that accommodates 18.2 ± 0.4 mm/yr of spreading associated with the divergent boundary separating the North American and Eurasian plates [DeMets

et al., 2010]. It consists of a central volcano along with an associated fissure swarm (Figure 6) that was the site of the most recent rifting episode, known as the Krafla Fires. The rifting episode occurred over a 9-year interval between 1975 and 1984 and included 9 eruptive and 20 diking events along a ~ 80 -km-long rift segment resulting in an average total opening of ~ 5 m [Tryggvason, 1984; Sigmundsson, 2006]. Subsequent deformation near Krafla has been observed using EDM, leveling, tilt, GPS, and InSAR [Foulger *et al.*, 1992; Tryggvason, 1994; Heki *et al.*, 1993; Hofton and Foulger, 1996; Pollitz and Sacks, 1996; Sturkell *et al.*, 2008; Ali *et al.*, 2010] and has been attributed to steady plate spreading, post rifting viscous relaxation (1984 onwards) along with inflation (between 1984–1989), and then deflation (1989 onwards) of the magma chamber beneath the caldera. Here, we focus on the deformation around the caldera of the central volcano caused by the deflating source during the 1990s [Sigmundsson *et al.*, 1997]. To describe the deformation, we once again employ the Mogi model [Mogi, 1958]. This application serves to validate our strategy on real data.

[24] We analyze synthetic aperture radar images acquired by the ERS-1 and ERS-2 satellites on 10 distinct epochs between 1993 and 1999 [Carr, 2008]. Figure 6 shows the geographic location of the subset of the ERS scene denoted by frame 2277

Table 2. ERS Data Used for Each Pair in This Study^a

Pair	h_a (m)	Species	First Epoch (t_i)		Second Epoch (t_j)		Span (days)
			Orbit	Year	Orbit	Year	
1	-2628.2	A	10174	1993.4822	17398	1998.6274	1879
2	-53.8	A	10174	1993.4822	5875	1996.4235	1074
3	-63.1	A	10675	1993.5781	11386	1997.4767	1424
4	64.9	A	10675	1993.5781	23410	1999.7781	2264
5	-198.6	B	11677	1993.7699	22408	1999.5863	2124
6	70.3	B	11677	1993.7699	6877	1996.6147	1039
7	190.2	A	5875	1996.4235	23410	1999.7781	1225
8	392.6	B	6376	1996.5191	22408	1999.5863	1120

^aThe term h_a denotes the altitude of ambiguity [Massonnet and Rabaute, 1993].

of Track 9. We combine $q = 10$ distinct epochs to form $c = 8$ interferometric pairs as listed in Table 2. These pairs form two independent sets, called “species” by Feigl and Thurber [2009], as shown in Figure 7. The eight pairs constitute a minimal set spanning the observed time interval, as shown by the lack of closed loops in the incidence graph. Topologically, the incidence graph for species I contains $q = 6$ nodes (corresponding to epochs) and $c = 5$ edges (corresponding to pairs). Similarly, species II contains $q = 4$ epochs and $c = 3$ pairs.

[25] To generate the interferograms, we use the DIAPASON InSAR processing software developed by the French Space Agency [Centre National

d'Etudes Spatiales, 2006]. The topographic contribution to the interferograms was removed using a digital elevation model (DEM) that has been resampled to 100-m posting and 20-m accuracy [Arnasson, 2006]. The observed wrapped phase change values for all 8 pairs are shown in Figure 9a. In these interferograms, one fringe of phase change corresponds to 28 mm of range change in the direction of the satellite. The principle signal in all eight interferograms is a concentric fringe pattern, consistent with volcanic deformation. We neglect the small contribution from steady plate spreading and post-rifting viscous relaxation as they contribute less than a quarter cycle (~ 7 mm) to the fringe pattern over the width of the study area in the

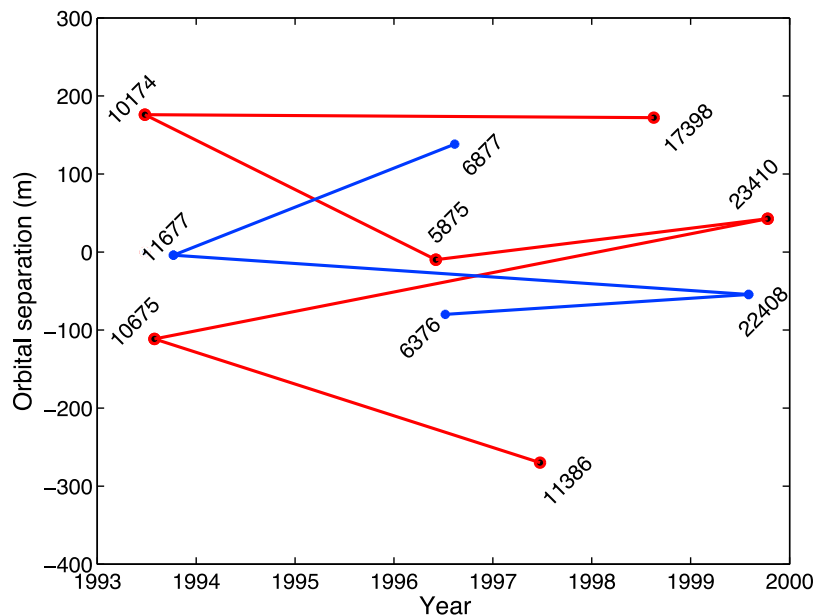


Figure 7. Orbital separation versus time for the interferograms. Horizontal axis displays the acquisition date (epoch) of each image, and labels next to circles denote orbit numbers and the vertical axis shows the orbital separation at the acquisition epoch. Dashed lines connect epochs used to form interferometric pairs in species I (red) and II (blue).

Table 3. Initial Estimate and Bounds for the Parameters Considered in the Inversion

Parameter Name	Initial p_0	Lower Bound p_L	Upper Bound p_U	Step δp
Easting (km)	599.0	597.0	607.0	0.5
Northing (km)	584.0	576.0	586.0	0.5
Depth (km)	4.0	2.0	7.0	0.5
$\Delta V/\Delta t$ ($10^6 \text{ m}^3/\text{yr}$)	-3.5	-5.0	0.0	0.1

interferogram spanning the longest time interval (~6 years) [Ali *et al.*, 2010].

[26] We now apply the strategy to estimate the four parameters in the Mogi model describing the

deflating source beneath the caldera of the Krafla central volcano from observed data. The InSAR data set for each pair spans 8 km in easting by 8 km in northing and includes 6400 pixels, reduced to $n < 500$ values of the range change gradient ψ by quadtree resampling. The initial estimate and bounds for the model parameters are the same for all pairs, as listed in Table 3. The bounds are fairly wide given the size of the image. Once again we deliberately choose a poor value for the initial estimate (Figure 8b). We perform the inversion using data from all pairs (1–8) as eight individual solutions and one ensemble solution. Results using pair 1 only are shown in Figure 8 and the values of estimated parameters are listed in the second column of Table 4. Figures 8a and 8e show the

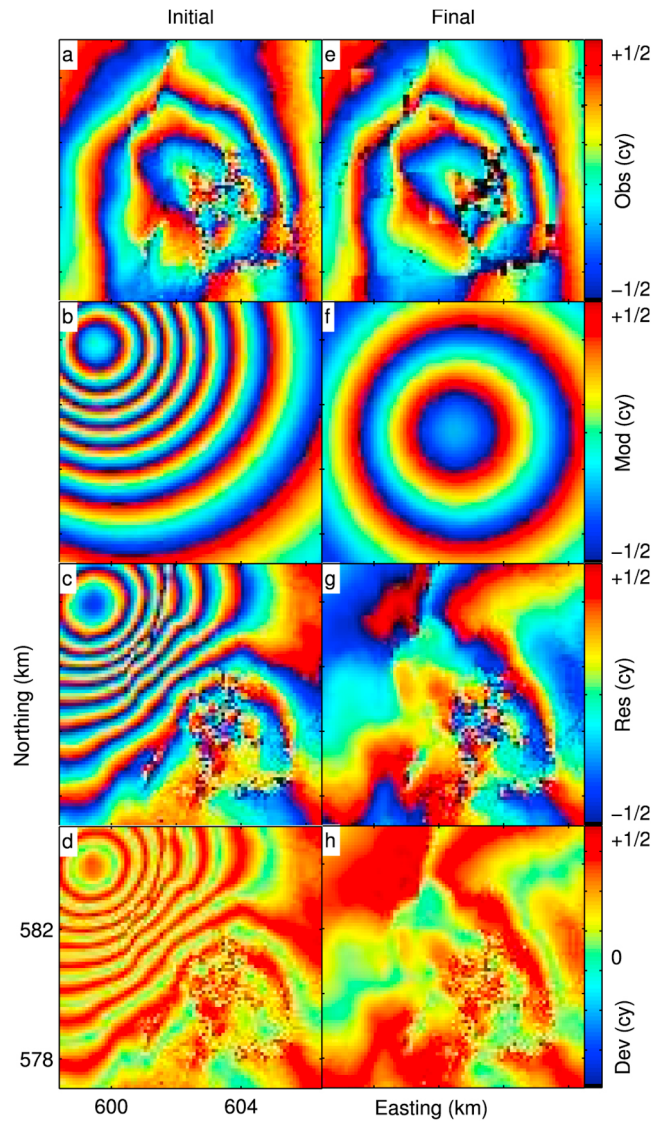


Figure 8. Interferograms for pair 1 spanning the 1993.48–1998.62 time interval. Plotting conventions as in Figure 1, except that Figures 8a and 8e show observed phase ϕ before and after quadtree resampling.

Table 4. Model Parameters Estimated Using Pair 1 and Pairs 1–8 (Individually and Jointly)

Parameter (Name)	Pair 1	Uncertainty (σ)	Pairs 1–8 (Mean)	Uncertainty (σ)	Pairs 1–8 (Joint)	Uncertainty (σ)
Easting (km)	601.954	314.5 (m)	601.746	96.0 (m)	601.605	44.1 (m)
Northing (km)	581.581	267.6 (m)	581.053	133.6 (m)	580.917	100.2 (m)
Depth (km)	3.480	224.9 (m)	4.437	318.0 (m)	4.975	208.1 (m)
$\Delta V/\Delta t$ ($10^6 \text{ m}^3/\text{yr}$)	-0.750	0.145	-1.144	0.208	-2.149	0.254

observed values of the phase field ϕ , before and after quadtree resampling, respectively. The modeled values of phase $\tilde{\phi}$ calculated using the initial and final estimates of the parameters are shown in Figures 8b and 8f, respectively. Figures 8c and 8g show the residual values between observed and modeled values for both the initial and final estimates, respectively. Figures 8d and 8h show the deviations between the observed and modeled values of the phase. During optimization, the cost decreases from $\bar{\omega}' = 0.105$ cycles per pixel for the initial estimate to $\bar{\omega}' = 0.066$ cycles per pixel for the final estimate.

[27] We repeat the same procedure for pairs 2 through 8. In all cases, we find that each parameter converges to a steady value after a few iterations. For brevity, we only show the range change field calculated from the final estimate (Figure 9b) and the corresponding range change residuals (Figure 9c) calculated by subtracting the modeled range change from the observed range change (Figure 9a). Figure 10 shows how the estimated parameters vary with different pairs. The weighted mean value for each of the parameters estimated from pairs 1–8 individually, is listed in the fourth column of Table 4. Pairs with large decorrelated regions result in a poor fit, increasing the uncertainty of the estimated parameters. We also perform an inversion of all eight pairs together as an ensemble. The values of estimated parameters, along with their uncertainties, are listed in the sixth and seventh columns of Table 4 and also plotted in Figure 10. For each parameter, the value estimated from the ensemble is similar to the mean value averaged over the eight pairs estimated individually.

7. Discussion

[28] The Mogi model describes most, but not all, of the observed deformation pattern, as indicated by the similarity between the observed and modeled values of the phase (Figures 9a and 9b,

respectively). Indeed, the residual values show little spatially coherent structure (Figure 9c). The remaining residuals could result from “nuisance effects”, inadequate parameterization of the source or processes such as plate-spreading and post-rifting relaxation that have been neglected in the model.

[29] Our estimates for easting and northing are similar to those estimated and used by Tryggvason [1999], Sigmundsson *et al.* [1997], and *de Zeeuw-van Dalsen et al.* [2004], but the depth estimate of 4.98 ± 0.21 km is deeper than previous estimates of 2–3 km. Most of the previous results are based on GPS data. Although *de Zeeuw-van Dalsen et al.* [2004] use a subset of the InSAR data analyzed here, they focus on a larger region and the central volcano is poorly resolved [*de Zeeuw-van Dalsen et al.*, 2004, Figures 2a–2h]. Using the conventional approach of unwrapping the interferometric phase and then estimating the parameters, they find a depth of 2.4 km for the shallow, deflating magma chamber. Some of the apparent discrepancy in depth can also be explained by differences in the elastic properties assumed for the modeling, as discussed previously by *Masterlark* [2007]. Our estimate, however, is consistent with results from seismic tomography that place the top and bottom of the magma chamber between 3 and 7 km below the surface, respectively [*Einarsson*, 1978; *Bransdottir et al.*, 1997].

[30] In terms of horizontal location of the source, the values of the Easting and Northing parameters estimated from the eight pairs individually agree within their uncertainties. Their weighted means agree with the values estimated from the eight-pair ensemble to within their uncertainties. The scaled standard error of the mean is 0.096 km and 0.133 km for the Easting and Northing parameters, respectively. These uncertainties are of the same order of magnitude as the bootstrap values of 0.044 km and 0.100 km from the eight-pair ensemble. The estimates of depth show more scatter. The mean of the depth estimates from the eight individual pairs,

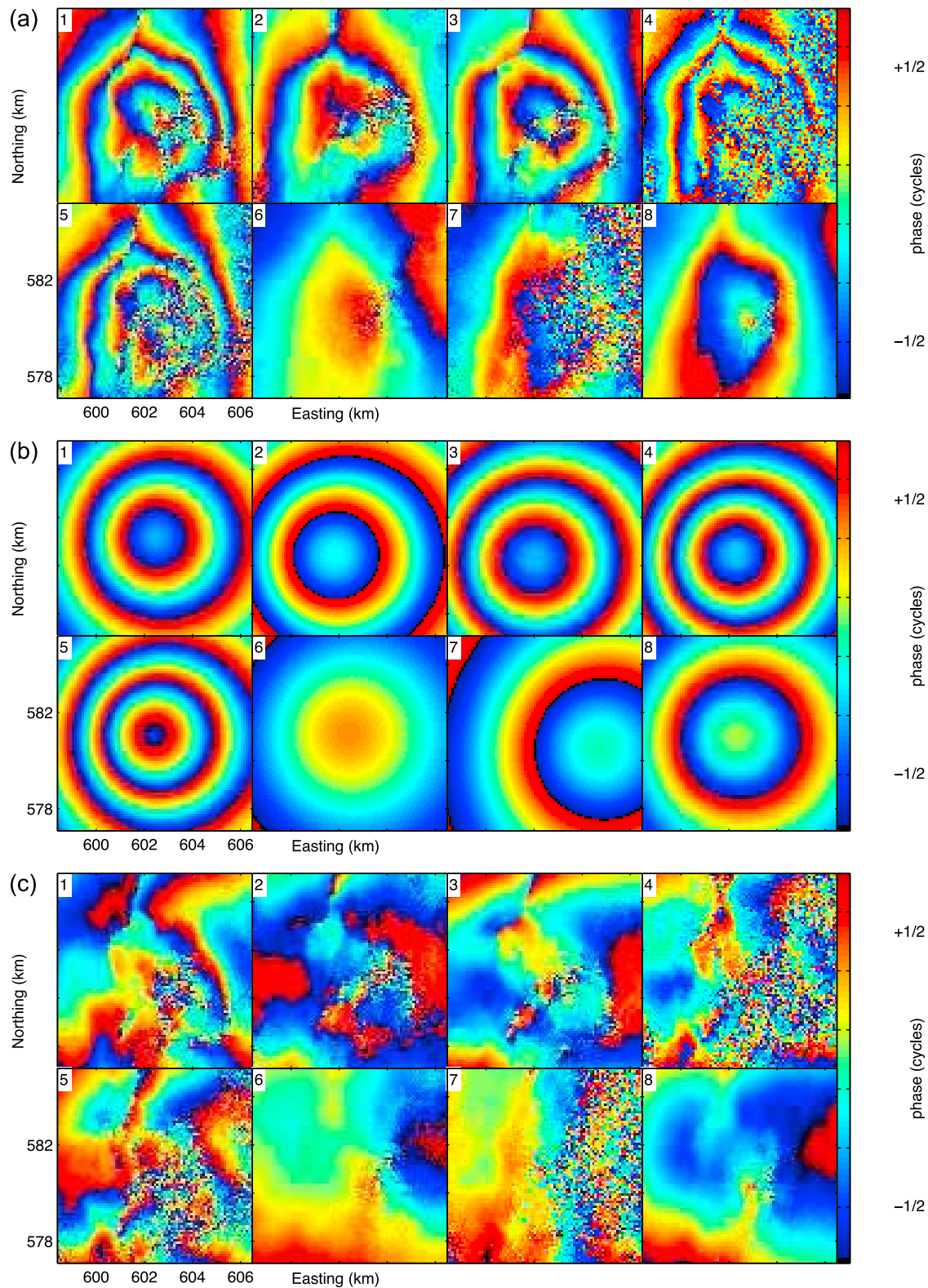


Figure 9. Interferograms showing wrapped phase values for pairs 1–8 listed in Table 2. (a) Observed phase values ϕ for pairs 1–8. (b) Modeled phase values ϕ for pairs 1–8, calculated using the final estimate from each pair. (c) Residual phase values θ for pairs 1–8, calculated as the wrapped difference of the observed and modeled values.

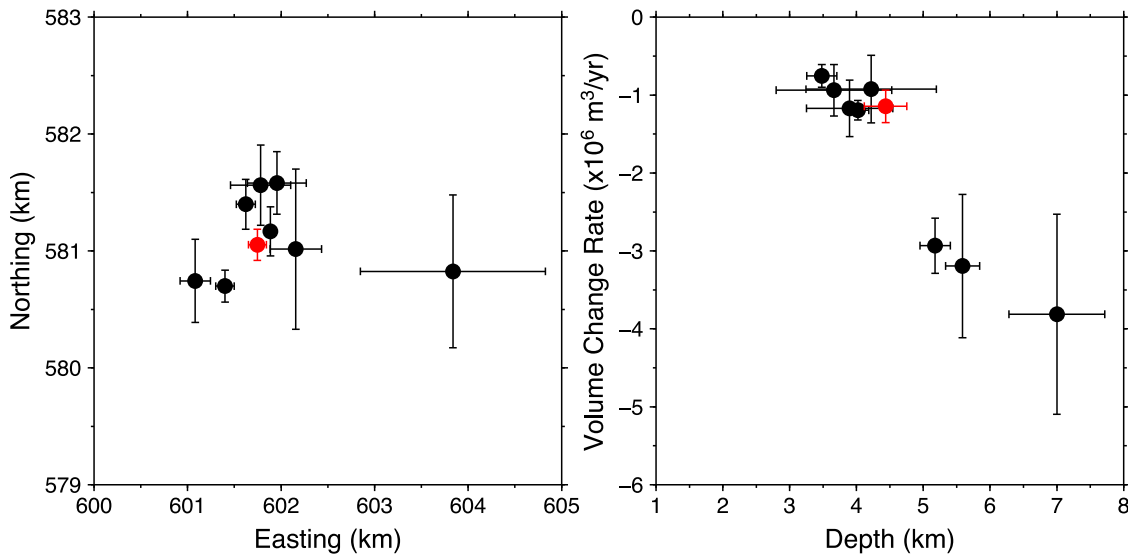


Figure 10. Final estimates of Mogi parameters for all eight pairs and their uncertainties. (a) Northing versus easting. (b) Volume change versus depth. Black dots represent the final estimates for each pair individually. Red dot represents final ensemble estimate using all eight pairs together. Bars indicate the $\pm 1\sigma$ bootstrap uncertainty.

4.44 ± 0.32 km, is within 2σ of the ensemble estimate of 4.98 ± 0.21 km.

[31] To compare our results to those of previous studies, we consider the rate of vertical displacement u_Z at a point located directly above the Mogi source. Figure 11 shows the vertical displacement as a function of time as estimated from pairs 1–8 individually. Following Sturkell *et al.* [2008], we

assume that u_Z decays exponentially as a function of time

$$u_Z(t_j, X_{Mogi}, Y_{Mogi})_{Z=0} = v_Z^{(0)}[\tau(1 - \exp(-(t - t_0)/\tau))] \quad (14)$$

where $t_0 = 1989.0$ is a reference epoch in years, corresponding to the beginning of the deflation of the volcano and $\tau = 4.39$ years is the

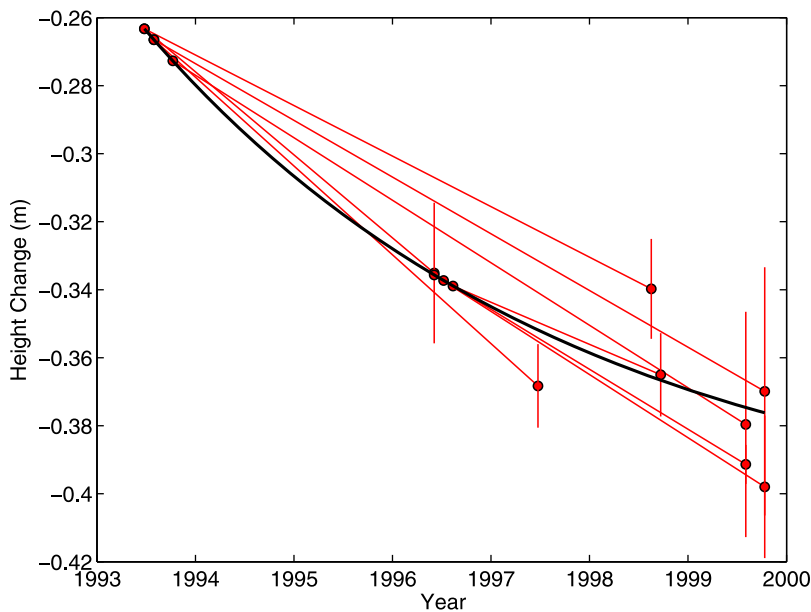


Figure 11. Vertical displacement u_Z as a function of time for a point located directly above the Mogi source estimated from pairs 1–8 individually (filled circles connected by solid red lines). Black line shows the exponential decay estimated by temporal adjustment, as described in the text.

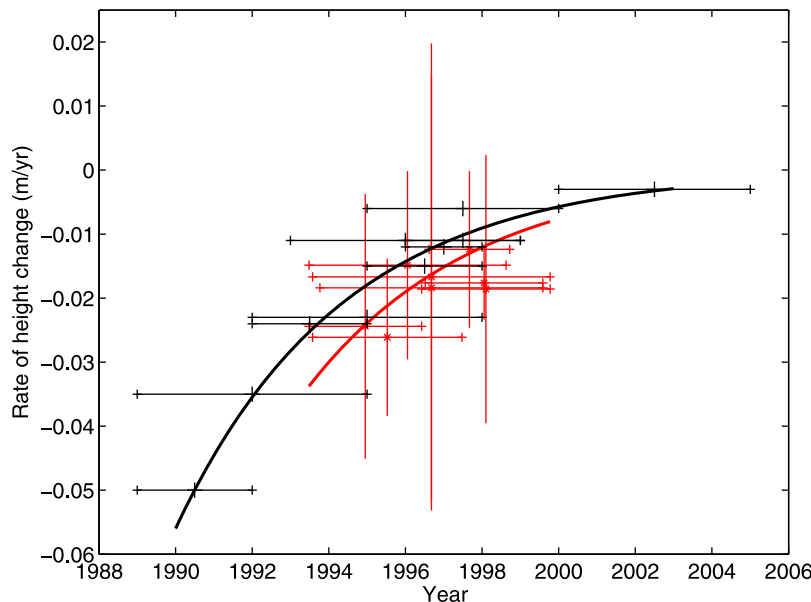


Figure 12. Vertical velocity v_z of a point located directly above the Mogi source as derived from InSAR (red crosses, this study) and previous studies (black crosses, Sturkell *et al.* [2008]). Horizontal bars indicate the time interval and vertical bars denote the uncertainty in the velocity. The red and black curves show exponential decay as estimated with temporal adjustment (this study) and a curve-fitting algorithm through the midpoints of the time intervals [Sturkell *et al.*, 2008], respectively.

characteristic decay time. To find the exponential curve that best fits the data, we estimate a single parameter by temporal adjustment of the linear system [Beauducel *et al.*, 2000; Feigl *et al.*, 2000; Schmidt and Bürgmann, 2003]. The best fitting value of $v_z^{(0)} = -0.0937$ m/yr leads to the curve in Figure 11. Taking the derivative with respect to time, we show the corresponding vertical velocity v_z as a function of time in Figure 12. The vertical velocity is negative, indicating subsidence. In magnitude, it slows from ~ 34 mm/yr in 1993 to ~ 8 mm/yr in 1999, in good agreement with the rates described by Sturkell *et al.* [2008].

8. Conclusions

[32] We have developed, validated, and applied a new strategy for estimating parameters in a geophysical model from the gradient of InSAR range change. This strategy offers a number of advantages. First, by working with range gradient, it avoids the pitfalls associated with phase unwrapping techniques. Second, the quadtree resampling algorithm adapts the sampling density to the spatial coherence in the interferogram. The size of patch determines the amount of spatial averaging or smoothing. For example, Figures 4a and 4e show the simulated wrapped phase values (with noise) before and after

quadtree resampling, respectively. The corresponding values of the range gradient appear in Figure 5a (Figure 5e is identical). Third, the method is also computationally efficient because the number of evaluations of the exact fitting function is $l(2m + 1)$, where l is the number of iterations and m is the number of parameters. The $(2m + 1)$ evaluations for each parameter can be performed independently, in parallel. Fourth, the procedure provides uncertainties for the estimated parameters via bootstrapping, without the need for additional evaluations of the exact fitting function. We have applied the strategy to estimate parameters of a deflating source beneath the Krafla central volcano using multiple interferometric pairs acquired by the ERS-1 and ERS-2 satellites over a 6-year interval between 1993 and 1999. The optimal solution estimated from the 8-pair ensemble indicates a source at 4.98 ± 0.21 km depth. Temporal adjustment of the eight pairs taken individually indicates a deflation rate that decays exponentially over the interval, in agreement with prior studies.

Acknowledgments

[33] We thank Cliff Thurber, Tim Masterlark, Freysteinn Sigmundsson and Peter Sobol for helpful discussions. ERS data were provided by the European Space Agency under the terms

and conditions of a Category-I project of which K. L. Feigl is a P.I. We also thank four anonymous reviewers for helpful comments that improved the clarity of the manuscript. This material is based upon work supported by the U.S. National Science Foundation award EAR-0810134.

References

- Ali, T., K. Feigl, C. H. Thurber, T. Masterlark, B. Carr, and F. Sigmundsson (2010), Geodetic measurements and models of rifting in northern Iceland for 1993–1998, Abstract G12A-05 presented at 2010 Fall Meeting, AGU, San Francisco, Calif., 13–17 Dec.
- Arnasson, K. (2006), A digital elevation model for Iceland with 25-m grid posting and 10-m accuracy, Natl. Land Surv. of Iceland, Reykjavik.
- Beauducel, F., P. Briole, and J. Froger (2000), Volcano wide fringes in ERS synthetic aperture radar interferograms of Etna: Deformation or tropospheric effect?, *J. Geophys. Res.*, **105**, 16,391–16,402.
- Bransdottir, B., W. Menke, P. Einarsson, R. S. White, and R. K. Staples (1997), Faroe-Iceland Ridge Experiment: 2. Crustal structure of the Krafla central volcano, *J. Geophys. Res.*, **102**, 7867–7886.
- Carr, B. B. (2008), Geodetic measurements and numerical models of rifting in northern Iceland for 1993–1999, M.S. thesis, Univ. of Wis.–Madison, Madison.
- Centre National d'Etudes Spatiales (2006), DIAPASON automated interferometric processing software, user's guide for version 4, Toulouse, France.
- DeMets, C., R. G. Gordon, and D. F. Argus (2010), Geologically current plate motions, *Geophys. J. Int.*, **181**(1), 1–80.
- de Zeeuw-van Dalfsen, E., R. Pedersen, F. Sigmundsson, and C. Pagli (2004), Satellite radar interferometry 1993–1999 suggests deep accumulation of magma near the crust–mantle boundary at the Krafla volcanic system, Iceland, *Geophys. Res. Lett.*, **31**, L13611, doi:10.1029/2004GL020059.
- Efron, B., and R. Tibshirani (1986), Bootstrap methods for standard errors, confidence intervals, and other measures of statistical accuracy, *Stat. Sci.*, **1**(1), 54–75.
- Einarsson, P. (1978), S-wave shadows in the Krafla Caldera in NE-Iceland: Evidence for a magma chamber in the crust, *Bull. Volcanol.*, **41**, 187–195.
- Feigl, K. L., and C. H. Thurber (2009), A method for modeling radar interferograms without phase unwrapping: Application to the M 5 FawnSkin, California earthquake of 1992 December 4, *Geophys. J. Int.*, **176**(2), 491–504.
- Feigl, K. L., J. Gasperi, F. Sigmundsson, and A. Rigo (2000), Crustal deformation near Hengill volcano, Iceland 1993–1998: Coupling between volcanism and faulting inferred from elastic modeling of satellite radar interferograms, *J. Geophys. Res.*, **105**(B11), 25,655–25,670.
- Fialko, Y. (2004), Evidence of fluid-filled upper crust from observations of post-seismic deformation due to the 1992 Mw7.3 Landers earthquake, *J. Geophys. Res.*, **109**, B08401, doi:10.1029/2003JB002985.
- Foulger, G., C. Jahn, G. Seeber, P. Einarsson, B. Julian, and K. Heki (1992), Post-rifting stress relaxation at the divergent plate boundary in northeast Iceland, *Nature*, **358**(6386), 488–490.
- Goffe, W. L. (1996), SIMANN: A global optimization algorithm using simulated annealing, *Stud. Nonlinear Dyn. Econom.*, **1**(3), 169–176.
- Heki, K., G. Foulger, B. Julian, and C. Jahn (1993), Plate dynamics near divergent plate boundaries: Geophysical implications of postripping crustal deformation in NE Iceland, *J. Geophys. Res.*, **98**(B8), 14,279–14,297.
- Hetland, E. A., P. Muse, M. Simons, Y. N. Lin, P. S. Agram, and C. J. DiCaprio (2012), Multiscale InSAR Time Series (MInTS) analysis of surface deformation, *J. Geophys. Res.*, **117**, B02404, doi:10.1029/2011JB008731.
- Hofton, M., and G. Foulger (1996), Postripping anelastic deformation around the spreading plate boundary, north Iceland: 1. Modeling of the 1987–1992 deformation field using a viscoelastic Earth structure, *J. Geophys. Res.*, **101**(B11), 25,403–25,421.
- Jonsson, S., H. Zebker, P. Segall, and F. Amelung (2002), Fault slip distribution of the 1999 M_w 7.1 Hector Mine, California, earthquake, estimated from satellite radar and GPS measurements, *Bull. Seismol. Soc. Am.*, **92**(4), 1377–1389.
- Kirkpatrick, S., C. D. Gelatt, and M. P. Vecchi (1983), Optimization by simulated annealing, *Science*, **220**(4598), 671–680.
- Kohlhase, A. O., K. L. Feigl, and D. Massonnet (2003), Applying differential InSAR to orbital dynamics: A new approach for estimating ERS trajectories, *J. Geod. Rev.*, **77**, 493–502.
- Lohman, R. B., and M. Simons (2005), Some thoughts on the use of InSAR data to constrain models of surface deformation: Noise structure and data downsampling, *Geochem. Geophys. Geosyst.*, **6**s, Q01007, doi:10.1029/2004GC000841.
- Malvern, L. E. (1969), *Introduction to Mechanics of a Continuous Medium*, 713 pp., Prentice-Hall, Englewood Cliffs, N. J.
- Mardia, K. V., and P. Jupp (2000), *Directional Statistics*, 2nd ed., John Wiley, Chichester, U. K.
- Massonnet, D., and K. Feigl (1998), Radar interferometry and its application to changes in the Earth's surface, *Rev. Geophys.*, **36**(4), 441–500.
- Massonnet, D., and T. Rabaute (1993), Radar interferometry—Limits and potential, *IEEE Trans. Geosci. Remote Sens.*, **31**(2), 455–464.
- Masterlark, T. (2007), Magma intrusion and deformation predictions: Sensitivities to the Mogi assumptions, *J. Geophys. Res.*, **112**, B06419, doi:10.1029/2006JB004860.
- Mogi, K. (1958), Relations between eruptions of various volcanoes and the deformations of the ground surfaces around them, *Bull. Earthquake Res. Inst. Univ. Tokyo*, **36**, 99–134.
- Nikolaidis, N., and I. Pitas (1998), Nonlinear processing and analysis of angular signals, *IEEE Trans. Signal Process.*, **46**, 3181–3194.
- Pollitz, F., and I. Sacks (1996), Viscosity structure beneath northeast Iceland, *J. Geophys. Res.*, **101**(B8), 17,771–17,793.
- Rennen, M. (2004a), Basics on coordinates and their reference, version 2.5, technical report, Landmaelingar Isl., Reykjavik.
- Rennen, M. (2004b), COCODATI: Coordinate conversion and datum transformation in Iceland (version 1.3), manual and technical reference, Landmaelingar Isl., Reykjavik. [Available at <http://cocolati.lmi.is/cocolati/cocodat-i.jsp>]
- Samet, H. (1984), The Quadtree and related hierarchical data structures, *ACM Comput. Surv.*, **16**(2), 187–260.
- Sandwell, D. T., and E. J. Price (1998), Phase gradient approach to stacking interferograms, *J. Geophys. Res.*, **103**(B12), 30,183–30,204.
- Savage, J. C. (1988), Principal component analysis of geodetically measured deformation in Long Valley caldera, eastern California, 1983–1987, *J. Geophys. Res.*, **93**, 13,297–13,305.
- Schmidt, D. A., and R. Bürgmann (2003), Time-dependent land uplift and subsidence in the Santa Clara valley, California,

- from a large interferometric synthetic aperture radar data set, *J. Geophys. Res.*, 108(B9), 2416, doi:10.1029/2002JB002267.
- Sigmundsson, F. (2006), *Iceland Geodynamics: Crustal Deformation and Divergent Plate Tectonics*, 209 pp., Springer, Berlin.
- Sigmundsson, F., H. Vadon, and D. Massonnet (1997), Readjustment of the Krafla spreading segment to crustal rifting measured by satellite radar sinterferometry, *Geophys. Res. Lett.*, 24(15), 1843–1846.
- Simons, M., Y. Fialko, and L. Rivera (2002), Coseismic deformation from the 1999 Mw 7.1 Hector Mine, California, earthquake as inferred from InSAR and GPS observations, *Bull. Seismol. Soc. Am.*, 92, 1390–1402.
- Sturkell, E., F. Sigmundsson, H. Geirsson, H. Olafsson, and T. Theodorsson (2008), Multiple volcano deformation sources in a post-rifting period: 1989–2005 behaviour of Krafla, Iceland constrained by levelling, tilt and GPS observations, *J. Volcanol. Geotherm. Res.*, 177(2), 405–417.
- Tryggvason, E. (1984), Widening of the Krafla fissure swarm during the 1975–1981 volcano-tectonic episode, *Bull. Volcanol.*, 47, 47–69, doi:10.1007/BF01960540.
- Tryggvason, E. (1994), Surface deformation at the Krafla Volcano, North Iceland, 1982–1992, *Bull. Volcanol.*, 56(2), 98–107.
- Tryggvason, E. (1999), The Krafla center of inflations and deflations during the years 1975 to 1997, *Res. Rep.*, 9901, Nord. Volcanol. Inst., Reykjavik.
- Wright, T. (2002), Remote monitoring of the earthquake cycle using satellite radar interferometry, *Philos. Trans. R. Soc. London, Ser. A*, 360(1801), 2873–2888.